Journal of Catalysis 260 (2008) 164–177

Contents lists available at ScienceDirect

Journal of Catalysis

www.elsevier.com/locate/jcat

The role of rhenium in the conversion of glycerol to synthesis gas over carbon supported platinum–rhenium catalysts

Edward L. Kunkes [a], Dante A. Simonetti [a], James A. Dumesic [a,*], William D. Pyrz [b], Luis E. Murillo [b], Jingguang G. Chen [b], Douglas J. Buttrey [b]

[a] *Department of Chemical and Biological Engineering, University of Wisconsin, Madison, WI 53706, USA*

[b] *Center for Catalytic Science and Technology, Department of Chemical Engineering, University of Delaware, Newark, DE 19716, USA*

ARTICLE INFO

Article history:
Received 13 August 2008
Revised 25 September 2008
Accepted 28 September 2008
Available online 16 October 2008

Keywords:
Glycerol
Reforming
Platinum
Rhenium
Bimetallic catalyst

ABSTRACT

Reaction kinetics measurements were carried out to study the conversion of aqueous solutions of glycerol (30 and 80 wt%) over carbon-supported Pt and Pt–Re catalysts at temperatures from 483 to 523 K. The results of these studies show that the turnover frequencies for production of H_2, CO, CO_2, and light alkanes (primarily methane) all increase upon the addition of Re to Pt/C catalysts. The molar ratio of H_2/CO increases, while the CO/CO_2 ratio decreases with Re addition, indicating increased rate of water–gas shift. For glycerol conversion over a Pt–Re/C catalyst with an atomic Pt:Re ratio of 1:1, increasing pressure or decreasing temperature leads to an increase in the production of alkanes and light oxygenated hydrocarbons (ethanol, methanol, propanediols, and acetone) at the expense of CO and CO_2. Temperature-programmed desorption studies and microcalorimetric measurements indicate that addition of Re to Pt modifies the interaction of CO with surface sites. X-ray absorption spectroscopy and transmission electron microscopy studies provide evidence indicating that Pt–Re/C catalysts consist primarily of bimetallic nanoparticles with sizes below 2 nm, and Re inhibits the sintering of these nanoparticles during reaction conditions for glycerol conversion. The results of these reaction kinetic studies and characterization studies indicate that the performance of Pt–Re/C catalysts for glycerol conversion is related to the formation of Pt–Re nanoparticles, for which Re promotes the overall rate of glycerol reforming by reducing the binding energy of CO to Pt, thereby leading to less extensive blocking of surface sites by reaction intermediates and/or products. In addition, the presence of Re facilitates water–gas shift and C–O bond cleavage reactions.

1. Introduction

The transportation sector requires fuels that burn cleanly and have high energy densities for efficient storage at ambient conditions. These criteria are currently best fulfilled by liquid hydrocarbons derived from petroleum. However, environmental and political concerns are driving society to develop alternative sources of transportation fuels. Biomass represents an attractive option for liquid fuels to supplement those derived from petroleum [1], provided that efficient and economical conversion technologies can be developed.

We have recently reported a low temperature process for the conversion of glycerol to synthesis gas over a carbon-supported Pt–Re catalyst [2,3]. Furthermore, we demonstrated that this glycerol conversion process can be combined with Fischer–Tropsch synthesis in a single reactor process such that the heat generated by the exothermic Fischer–Tropsch reaction can be supplied to the endothermic glycerol reforming reaction [4]. This combined process allows for the direct production of liquid alkanes suitable for transportation applications from glycerol [4]. Previous reaction kinetics studies showed that the addition of Re to Pt increased the catalytic activity by an order of magnitude compared to monometallic Pt catalysts at conditions leading to high coverages of CO [2]. Temperature-programmed reduction studies revealed that Pt and Re formed an alloy [2], and it was suggested that one of the roles of Re is to reduce the binding energy of CO to Pt, thereby allowing the catalyst to operate with high rates under high partial pressures of CO [2].

In this study, we investigate in more detail the role of Re in carbon-supported PtRe catalysts. Reaction kinetics studies were conducted at various conditions over monometallic Pt/C and various Pt–Re/C catalysts to identify the effects of process conditions and Re addition on reaction pathways for glycerol reforming. Microcalorimetric measurements and CO temperature-programmed desorption (CO-TPD) studies were conducted to determine the effect of Re on the catalyst surface, and X-ray absorption spec-

---

[*] Corresponding author.
E-mail address: dumesic@engr.wisc.edu (J.A. Dumesic).

0021-9517/$ – see front matter © 2008 Elsevier Inc. All rights reserved.
doi:10.1016/j.jcat.2008.09.027

troscopy (XAS) and transmission electron microscopy (TEM) studies were conducted to characterize the bulk properties of the catalyst (i.e., alloy formation, particle size, and composition).

2. Experimental

2.1. Catalyst preparation

Carbon-supported Pt and Re catalysts were prepared by incipient wetness impregnation of carbon black (Vulcan XC-72) with aqueous solutions of $H_2PtCl_6{\cdot}6H_2O$ and $HReO_4$ (Strem Chemicals), respectively. The carbon-supported bimetallic Pt–Re catalysts were prepared by impregnating the support with an aqueous solution of both $H_2PtCl_6{\cdot}6H_2O$ and $HReO_4$. The support was dried in air for 12 h at 373 K prior to impregnation, and 1.7 g of solution were used for every gram of support. The catalyst was dried at 403 K for 12 h in air after impregnation. Prior to reaction kinetics measurements, the catalysts were reduced in H_2 (180 cm^3(STP) min^{-1} for 2 h at 723 K (0.5 $K\,min^{-1}$) for Pt–Re/C or 533 K (0.5 $K\,min^{-1}$) for Pt/C). The adsorption uptakes of carbon monoxide and H_2 at 300 K were measured previously on a standard gas adsorption apparatus, and the number of catalytic sites was taken to be equal to the irreversible CO uptake [2]. We have demonstrated with CO chemisorptions, that the effect of reduction temperature on the catalyst dispersion is not significant in the range of reduction temperatures used to prepare the aforementioned catalysts.

2.2. Temperature-programmed desorption

Carbon monoxide temperature-programmed desorption (CO-TPD) experiments were carried out using an apparatus consisting of a mass flow controller (Teledyne-Hastings) and tube furnace connected to a variable power-supply and PID temperature controller (Love Controls) with a K-type thermocouple (Omega). The effluent was monitored by a mass spectrometer system consisting of a quadruple residual gas analyzer (Stanford Instruments RGA 200) inside a vacuum chamber. Vacuum was provided by a diffusion pump connected in series to a rotary pump. The effluent was introduced into the vacuum chamber via a constricted quartz capillary, resulting in a pressure of 5×10^{-5} Torr inside the chamber. Dried, unreduced catalyst samples were loaded into a 12.6 mm (0.5 inch) outer diameter, fritted quartz tube reactor. Prior to desorption experiments, 0.1 g of catalyst was reduced in flowing hydrogen (100 cm^3(STP)$\,min^{-1}$) for 2 h. The Pt/C and Re-containing catalysts were reduced at 533 and 723 K, respectively. The catalysts were degassed for 1 h in flowing helium (200 cm^3(STP) min^{-1}) at the reduction temperature, and then cooled to 300 K. Carbon monoxide was adsorbed onto the reduced catalysts by exposure to flowing 10 mol% CO in helium (100 cm^3(STP)$\,min^{-1}$) for 15 min. Residual CO was removed by purging the catalyst with helium (200 cm^3(STP)$\,min^{-1}$) at 300 K for 2 h. Desorption of CO was performed by heating the catalyst at a rate of 10 K min^{-1} under flowing helium (100 cm^3(STP)$\,min^{-1}$) from room temperature to 973 K.

2.3. X-ray absorption studies

X-ray absorption spectroscopy (XAS) data were collected in transmission mode on beamline X18-B at the National Synchrotron Light Source (NSLS), Brookhaven National Laboratory. The station uses a double crystal Si(111) monochromator which yields an energy range of 4.8–40 keV and focuses 1 mrad of radiation onto a 1.5 mm by 2.5 mm sample spot. The monochromator possesses an energy resolution of 1×10^{-4} $eV\,eV^{-1}$. For all Re-containing samples, the Re L_{III} absorption edge was measured from 200 eV below to 1240 eV ($k = 18$ Å^{-1}) above the edge position (10535 eV). For samples containing only Pt, the Pt L_{III} edge was measured from 150 eV below to 1240 eV ($k = 18$ Å^{-1}) above the edge position (11564 eV). For samples containing both Pt and Re, the Pt L_{III} edge measurement was truncated at 310 eV ($k = 9$ Å^{-1}) above the edge position, because of interference from the Re L_{II} edge at 11959 eV. Platinum and rhenium foils were used as references for energy calibration of the Pt L_{III} and Re L_{III} edge measurements in the transmission mode, respectively.

Prior to analysis, all catalyst samples were reduced in flowing hydrogen at 723 K for Re-containing samples and 533 K for Pt/C. One sample of Pt–Re(1:1)/C was exposed to more harsh reaction conditions for glycerol reforming (20 bar, 548 K, 0.08 $mL\,min^{-1}$ 80 wt% glycerol). All catalyst samples were purged with helium and passivated at room temperature with 2 mol% O_2 in He. Samples for XAS measurements were prepared by pressing 0.1–0.2 g of each catalyst sample into a self-supporting wafer, which was loaded into a special X-ray transparent cell [5] for pretreatment. The thickness of each wafer corresponded to 1–2 absorption lengths as measured near the Pt or Re L_{III} edge. For most samples, XAS measurements were performed both before and after in situ reduction in flowing hydrogen (5 mol% in N_2) at 533 K. The Pt L_{III} edge, Re L_{III} edge, or both absorption edges were scanned 3–5 times. Kapton-tape-mounted samples of platinum and rhenium salts/oxides were prepared by a method described elsewhere [6] and mounted directly onto the slit of the first ion chamber. All X-ray absorption data were collected at room temperature and in the presence of flowing hydrogen (5 mol% in N_2). We have confirmed that there is no significant difference between the performance of catalysts that have been exposed to reaction conditions immediately after undergoing reduction in neat hydrogen and those exposed to a subsequent passivation followed by dilute hydrogen treatment at 533 K, with the latter being used as the reduction conditions for XAS measurements.

The XAS data were processed and analyzed using ATHENA and ARTEMIS analysis software packages [7]. Data processing in ATHENA included removal of a smooth atomic background function and subsequent normalization of the raw absorption data. For the purposes of background removal and edge energy determination, the absorption edge energy, E_0, was taken as the position of the maximum of the first derivative in the range from 50 eV below to 50 eV above the nominal edge position. The normalized EXAFS data were weighted by k^3 and Fourier-transformed from k-space into R-space to yield the phase-uncorrected radial distribution function (RDF). The range of the Fourier transform was 3.0–14.0 Å^{-1} for the Re L_{III} edge and 3.0–9.0 Å^{-1} for the Pt L_{III} edge. For the monometallic catalyst samples, the normalized EXAFS signal was fitted in R-space using ARTEMIS. The theoretical standards for Pt–Pt and Re–Re single scattering were generated with the FEFF 6.0 code using structural information for Pt and Re, respectively [8]. Amplitude reduction factors (S_0^2) for Pt and Re were determined by fitting the theoretical standards to EXAFS data of the respective foil reference.

2.4. Transmission electron microscopy

Transmission electron microscopy (TEM) analyses were performed on a JEOL-2010F equipped with a Schottky field-emission gun operated at 200 keV with an ultrahigh resolution pole piece, providing a point resolution of 1.9 Å. Annular dark field (ADF) imaging was performed using a 0.5 nm or 0.7 nm diameter nanoprobe at camera lengths of 8–20 cm. Energy dispersive X-ray spectroscopy (EDS) was used to obtain elemental analysis with an EDAX Phoenix X-ray spectrometer with a resolution of 134 eV over a 40 keV range. EDS analysis was performed in STEM mode using a 0.5 to 0.7 nm diameter nanoprobe. Pt and Re L lines were used to quantify the relative abundances of Pt and Re, respectively.

Table 1
Properties of Pt and Pt–Re catalysts used during kinetics experiments. Adapted from Simonetti et al. [2].

Catalyst	Pt loading (wt%)	Re loading (wt%)	Bulk atomic Pt:Re ratio	Irreversible		CO:(total metal) atomic ratio	CO:H uptake ratio
				CO uptake (μmol g^{-1})	H uptake (μmol g^{-1})		
Re/C	–	5.0	–	30	–	0.10	–
Pt/C	5.0	–	–	130	130	0.53	1.0
Pt–Re/C	5.1	4.9	1:1	150	64	0.29	2.3
Pt–Re/C	5.1	0.5	10:1	120	90	0.40	1.3
Pt–Re/C	3.4	6.6	1:2	64	48	0.12	1.3

Table 2
Results from reaction kinetics experiments of carbon supported Pt and Pt–Re catalysts under clean and harsh reaction conditions.

Catalyst	Condition[a]	TOF (min^{-1})				Molar ratios			Carbon	
		H_2	CO	CO_2	Alkanes[b]	H_2/CO	CO/CO_2	CO/$C_{alkanes}$	As gas phase species (%)	As liquid phase species[c] (%)
Pt	Clean	3.1	2.8	0.019	0.32	1.1	147	8.8	54	46
Pt–Re(10:1)	Clean	5.6	5.2	0.031	0.48	1.1	165	11	81	19
Pt–Re(1:1)	Clean	7.4	4.1	1.3	0.31	1.8	3.2	14	99.5	0.5
Pt–Re(1:2)	Clean	20	4.6	7.2	0.78	4.3	0.65	5.3	99	1.1
Pt–Re(1:1)	Harsh	2.3	1.9	0.63	0.48	1.2	3.0	3.9	44	56

[a] Clean reaction conditions are 548 K, atmospheric pressure, 0.08 mL min^{-1} of 30 wt% glycerol feed, and 1.0 g catalyst (WHSV = 1.6 h^{-1}). Harsh reaction conditions are 548 K, 10.7 bar, 0.04 mL min^{-1} of 80 wt% glycerol feed, and 1.0 g catalyst (WHSV = 2.3 h^{-1}).

[b] Methane, ethane, and propane.

[c] Methanol, ethanol, acetone, acetol, propanediols, and glycerol.

Reduced and passivated carbon-supported catalyst samples (fresh and after exposure to reaction conditions) were prepared by dipping a lacey-carbon coated Cu grid into the sample powder.

2.5. *Microcalorimetry*

Microcalorimetric measurements of CO adsorption were performed at 300 K using a Setaram BT2 15D heat-flux calorimeter. The Pt/C catalyst was reduced in flowing H_2 (200 cm^3(STP) min^{-1}) for 2 h at 533 K. The Re-containing catalysts were reduced for 2 h at 723 K. Reduction was followed by treatment in flowing helium for 2 h at 723 K. The sample was then sealed under 350 Torr of He in a Pyrex capsule, and the capsule was loaded into a set of calorimetric cells. After the sample and cell reached thermal equilibrium with the calorimeter, the capsule was broken and microcalorimetric measurements were made by sequentially introducing small doses ($\sim$1 μmol g^{-1}) of CO onto the sample. The heat signal was recorded as a function of time, and this signal was integrated to obtain the energy released per dose. Volumetric measurements were made to determine the amount of gas adsorbed during the dose, using the dosing pressure, equilibrium pressure, system volumes, and temperature. A more detailed description of the procedure is given by Spiewak et al. [9].

2.6. *Reaction kinetics studies*

Reaction kinetics studies were conducted on an apparatus described elsewhere [4]. The reactor consisted of a 12.6 mm (0.5 inch) outer diameter stainless steel tube with a wall thickness of 0.71 mm (0.028 inch). A bed consisting of fresh powdered catalyst (1 or 3 g) mixed with an equal volume of fused SiO_2 granules ($-4+16$ mesh; Sigma Aldrich) was loaded between a quartz wool plug and fused SiO_2 granules. The reactor was heated with a furnace consisting of a close fitting aluminum block heated externally by a well-insulated furnace (1450 W/115 V, Applied Test Systems series 3210). A type K thermocouple (Omega) was attached to the outside of the reactor to measure temperature, which was controlled with a 1600 series type temperature controller (Dwyer Instruments). Liquid feed solutions were introduced into the reactor, with or without gas co-feed, in a down-flow configuration. The liquid feed flowrate was controlled with an HPLC pump (Alltech Model 301) and entered a syringe needle (Hamilton; point 5 tip) to introduce droplets of the feed into the reactor. The flow of gas (H_2 for reduction) was controlled with a Brooks 5850 model mass-flow controller. The effluent liquid was condensed in a gas–liquid separator and drained periodically for gas-chromatograph (GC) analysis (Agilent 6890 with a flame ionization detector, FID, and HP-Innowax column). Each effluent was tested for the presence of oxygenated hydrocarbons. The effluent gas stream passed through a back-pressure regulator (GO Regulator, Model BP-60) to maintain the system pressure, and the gas was analyzed for CO, CO_2, and light alkanes (C_1–C_3) using an HP-5890 GC with thermal conductivity detector (TCD) and a Haysep DB 100/120 column (Alltech). A Carle GC 8700 with TCD was used to analyze H_2 in the effluent gas. The weight hourly space velocity (WHSV) was calculated as the total mass flowrate of glycerol into the reactor divided by the total mass of catalyst. “Clean” reaction conditions refer to atmospheric pressure with a flowrate of 0.08 mL min^{-1} of a 30 wt% glycerol feed at 548 K and “harsh” reaction conditions refer to 10.7 bar pressure with a flowrate of 0.04 mL min^{-1} of an 80 wt% glycerol feed at 548 K. Each set of conditions was tested for at least 24 h time-on-stream, and the carbon balance for each condition closed to within 10%.

3. Results and discussion

3.1. *Reaction kinetic studies*

Table 1 lists the characteristics of the Pt/C, Re/C, and Pt–Re/C catalysts used in this study [2]. Previous studies suggest that Pt and Re form an alloy in the bimetallic catalysts and that the role of Re is to lower the binding energy of CO on Pt sites, thereby increasing catalytic activity at low temperatures [2,3]. To investigate the effects of reaction conditions on Pt/C and Pt–Re/C catalysts and to elucidate further the role of Re, reaction kinetics studies were conducted of carbon-supported Pt and Pt–Re bimetallic catalysts at 548 K under clean conditions, as well as reaction kinetics studies of the Pt–Re(1:1)/C catalyst at 548 K under harsh reaction conditions. The values of turnover frequency (TOF), molar ratios, and carbon conversions are listed in Table 2. One gram of catalyst was used for each experiment corresponding to a WHSV of 1.6 h^{-1} for clean conditions and 2.3 h^{-1} for harsh conditions.

Addition of Re to Pt under clean reaction conditions provided an increase in the turnover frequency and thus the conversion to

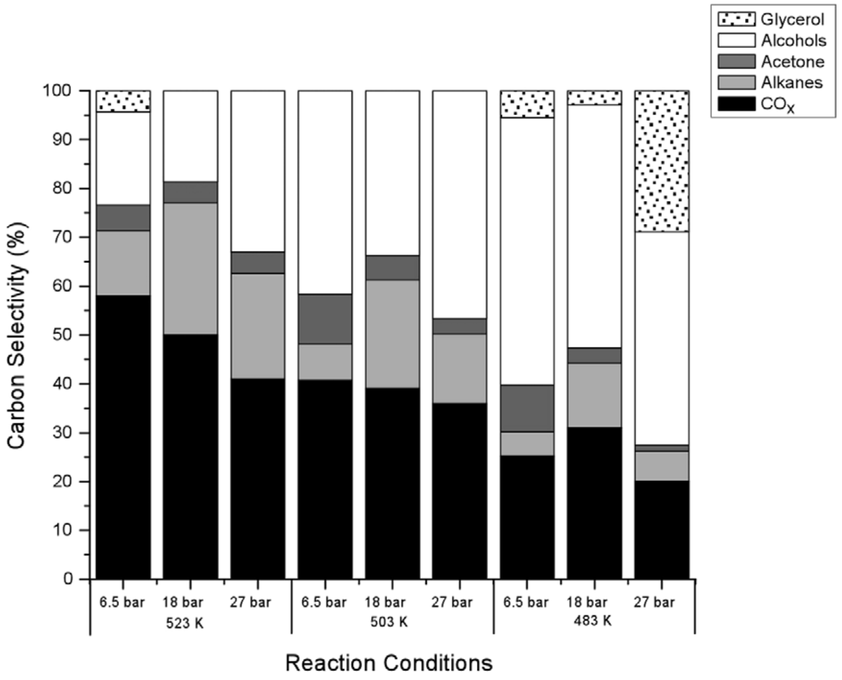

Fig. 1. Carbon selectivities versus temperature and pressure for conversion of glycerol over 5.1 wt% Pt–4.9 wt% Re/C (Pt/Re(1:1)/C). Reactions carried out using 0.04 $mL\,min^{-1}$ of 80 wt% glycerol feed and 3.0 g catalyst (WHSV = 0.75 h^{-1}).

Table 3

Molar carbon ratios as a function of temperature and pressure for the conversion of glycerol over 5.1 wt% Pt–4.9 wt% Re/C. Reaction conditions as in Fig. 1.

	6.5 bar	18 bar	27 bar
(A) 523 K			
CO_x/alkanes	4.36	1.86	1.91
CO_x/(alcohol + ketone)	2.39	2.18	1.1
$CO/CO_2 \times 10$	8.32	0.75	0.32
(B) 503 K			
CO_x/alkanes	5.52	1.77	2.53
CO_x/(alcohol + ketone)	0.79	1.01	0.72
$CO/CO_2 \times 10$	5.73	0.58	0.28
(C) 483 K			
CO_x/alkanes	5.06	2.35	3.28
CO_x/(alcohol + ketone)	0.39	0.59	0.45
$CO/CO_2 \times 10$	1.79	0.16	0.08

gas phase species. The turnover frequencies for H_2 and CO production increase by a factor of 2 upon addition of Re for an atomic Re:Pt ratio of 1/10 and an equimolar amount of Re to Pt. Addition of twice the amount of Re to Pt results in a factor of 8 increase in the H_2 TOF and a factor of 2 increase in CO TOF. The turnover frequencies for CO_2 production are similar for the monometallic Pt and Pt–Re(10:1) catalysts; however, higher Re loadings show a significant increase in CO_2 production (two orders of magnitude). The alkane production rate is similar for Pt, Pt–Re(10:1), and Pt–Re(1:1), but it increases by a factor of two for Pt–Re(1:2). Increasing Re content under clean reaction conditions leads to an increase in the H_2/CO molar ratio and a decrease in the CO/CO_2 molar ratio. The H_2/CO ratio is the same for Pt and Pt–Re(10:1), but it increases by a factor of 2 for Pt–Re(1:1) and a factor of 4 for Pt–Re(1:2). Similarly, the CO/CO_2 ratio is the same for the Pt and Pt–Re(10:1) catalysts, but it decreases by two orders of magnitude for Pt–Re(1:1) and three orders of magnitude for Pt–Re(1:2).

The above results show that the activities of the Pt and Pt–Re (10:1) catalysts are similar, indicating that the Pt surface is not affected significantly by the addition of a small amount of Re [2]. However, a 1:1 or 1:2 Pt:Re ratio leads to increased catalytic activity and a shift in selectivity. Previous studies have shown that the reaction pathways of oxygenated hydrocarbons (with a C:O stoichiometry of 1:1) involve dehydrogenation and C–C bond cleavage to form H_2 and adsorbed CO species, which further react to form H_2/CO_2 via water–gas shift (WGS) or CH_4 via methanation [10,11]. Also, these molecules can undergo C–O bond cleavage followed by hydrogenation to form alkanes and oxygenated hydrocarbons with $C{:}O > 1$ [10,11]. Addition of Re to Pt leads to a decrease in the value of the CO/CO_2 ratio, indicating that Re facilitates conversion of CO to CO_2 via WGS. The process conditions also affect the catalytic performance and therefore, the reaction pathways. The decreases in conversion to gas phase species and CO/C_{alkanes} ratio with increasing pressure and/or glycerol feed concentration indicate that these process conditions favor C–O bond cleavage as opposed to C–C bond cleavage.

Reaction kinetics studies of the Pt–Re(1:1)/C catalyst under conditions similar to the harsh conditions in Table 2 were conducted to elucidate further the role of Re addition. Fig. 1 shows the effect of varying pressure on carbon selectivities for the conversion of an 80 wt% glycerol solution at temperatures between 483 and 523 K over 3 g of PtRe(1:1)/C catalysts (WHSV = 0.75 h^{-1}). At constant temperature, an increase in pressure from 6.5 bar to 18 bar results in an increase in alkane production at the expense of CO_x species, alcohols/diols, and acetone. However, at 27 bar, the production of oxygenated hydrocarbons in the aqueous phase increases while the production of gaseous species (alkanes and CO_x) decreases. The increase in oxygenated hydrocarbons indicates a shift in selectivity from C–C bond breaking to C–O bond breaking at elevated pressures. As pressure increases, the rate of C–O bond cleavage slows, and the production of more oxygenated species (alcohols) becomes favored over the formation of alkanes.

The values of the CO_x/(alcohol + ketone) and CO_x/alkane ratios listed in Table 3 decrease with increasing pressure, further showing the shift in selectivity from CO_x species via C–C cleavage to oxygenated hydrocarbons and alkanes via C–O bond cleavage. The decrease in CO/CO_2 ratio indicates an increase in the rate of WGS at higher partial pressures of water. Decreasing temperature at constant pressure has a similar effect as increasing pressure. The rates of CO and CO_2 production decrease with an increase in the production of alkanes and oxygenates in the aqueous phase, thus indicating a shift from C–C scission to C–O scission. As mentioned previously, high rates of C–C bond cleavage lead to the production of gaseous CO/CO_2 and high rates of C–O bond cleavage favor the production of alkanes. As temperature decreases, the value of the CO_x/(alcohol + ketone) ratio decreases and the CO_x/alkane ratio remains unchanged, indicating that decreasing temperature favors the formation of alcohols, diols, and acetone, similar to the effect of increasing pressure. The observation of unreacted glycerol at low temperature (483 K) and high pressure (27 bar) further indicates the decrease in the rates of both C–C and C–O bond scission at these conditions.

3.2. *X-ray absorption spectroscopy*

XAS scans of Pt L_{III} and Re L_{III} edges were performed on Pt/C, PtRe/C(1:1), PtRe/C(1:1) after harsh reaction and Re/C catalysts, before and after in situ reduction inside the XAS cell. The catalysts were scanned prior to in situ reduction to determine the effect of oxygen passivation on the individual metal components. These results allow us to utilize this reaction of oxygen with the surface/bulk of the catalysts as a means of characterization.

Fig. 2 shows the Pt and Re L_{III} edge energy shifts for various samples as compared to bulk Pt and Re foils, respectively. Various investigators have found a relationship between metal oxidation state and the energy shift of the absorption edge [12–15]. In Fig. 2, a linear fit is constructed through L_{III} energy shifts of Pt and Re compounds with known metal oxidation states, with additional points representing measured energy shifts of catalyst samples before and after the in situ reduction. The small energy shifts (<0.5 eV) observed in the Pt and Re edges of the in situ reduced catalyst samples are within the experimental error of the technique and suggest that both metals are completely reduced during the pre-treatment. TPR measurements conducted previously also indicate complete reduction of both metals [2]. Fig. 2 shows that the degree of re-oxidation (caused by the passivation procedure), as indicated by the energy shifts in the samples before in situ reduction, is more significant for Re than for Pt in all catalyst samples. This observation is in agreement with the higher oxygen affinity of Re as compared to Pt [16]. The passivation procedure likely causes the oxidation of existing surface rhenium, and may induce segregation of bulk Re onto the particle surface, leading to further oxidation. Additional means of oxidation are provided by diffusion of oxygen into the bulk of the metal particles. The tendency towards oxidation by either of the pathways described above is likely to increase with increasing metal dispersions. It is interesting to note that the extent of Re re-oxidation is higher for fresh Pt–Re(1:1)/C than Pt–Re(1:1)/C after exposing to harsh conditions, and that the degree of oxidation is lowest for Re/C. Results from CO chemisorption and TEM measurements reveal that the dispersion of Pt–Re(1:1)/C (30%) is significantly higher than that of monometallic Re/C (10%) (see Table 1) [2]. Therefore, it is likely that the small particles of the bimetallic catalyst contain highly dispersed Re which is more susceptible to oxidation than the bulk Re found in the monometallic sample. Based on this relationship between particle size and the extent of Re re-oxidation, one can conclude that exposure to harsh reaction conditions decreases the dispersion of Re in the catalyst.

The presence of rhenium in an oxidized state is evident in the Fourier transform (Fig. 3) of the Re L_{III} edge EXAFS of the catalysts before in situ H_2 pre-treatment. In studies of alumina supported Pt–Re catalysts, Rønning, et al. have identified that the resonance at 1.5 Å results from first coordination shell Re–O scattering with $R_{\text{Re–O}} = 1.72$ Å, and the resonances between 2 and 3 Å result from scattering by other metal atoms (Pt or Re) in the first coordination shell [17]. A similar Re–O scattering resonance is seen in NH_4ReO_4, with $R_{\text{Re–O}} = 1.74$ Å [17]. In Fig. 3, the size of the Re–O resonance increases when going from Re/C to Pt–Re(1:1)/C after reaction to Pt–Re(1:1)/C, a trend that is also found in the Re L_{III} edge energy shifts (Fig. 2). Both Re/C and Pt–Re(1:1)/C after reaction show considerable Re–metal interaction as indicated by the Fourier transform magnitude between 2–3 Å. In contrast, Pt–Re(1:1)/C shows little magnitude in this region, and its Fourier transform closely resembles that of Re in NH_4ReO_4, suggesting near-complete re-oxidation. In summary, analysis of the XAS data collected from catalyst samples prior to in situ reduction demonstrates that in the presence of platinum, rhenium is highly dispersed, and that harsh reaction conditions tend to decrease Re dispersion.

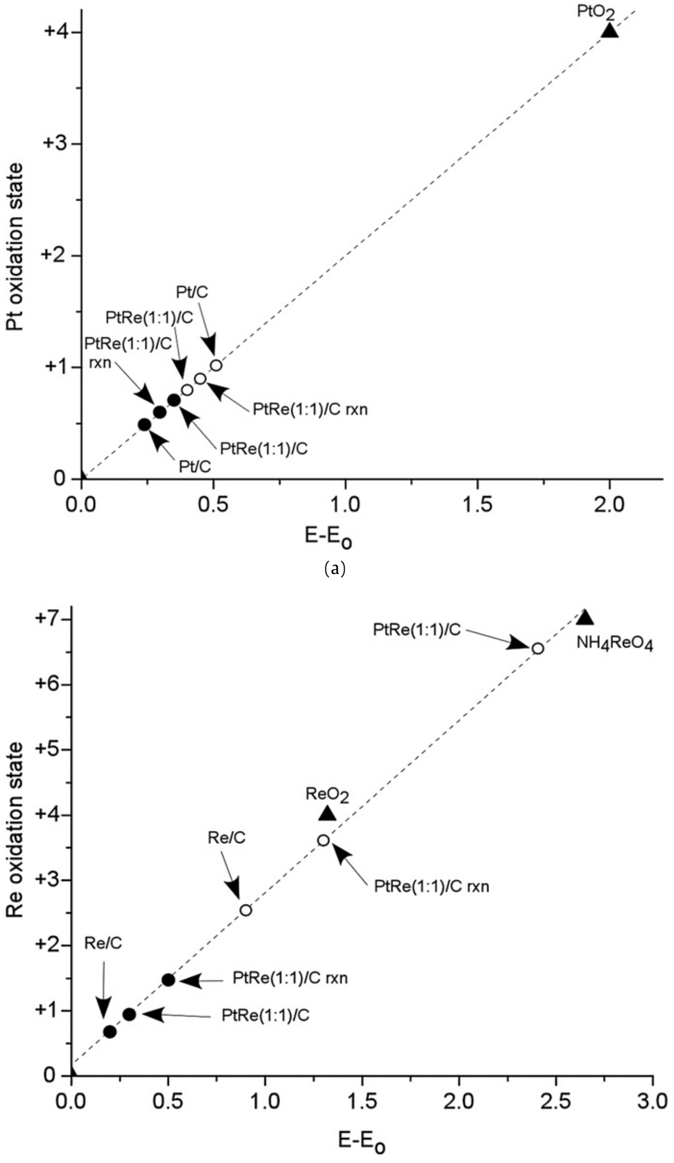

Fig. 2. XANES measurements of the (a) Pt L_{III} edge and (b) Re L_{III} edge. Filled circles are reduced samples, open circles are samples before in situ reduction, and triangles are standards. "PtRe(1:1)/C-rxn" represents a catalyst that was exposed to "harsh" reaction conditions.

The proximity of the atomic numbers of platinum and rhenium causes the two elements to possess similar EXAFS back-scattering amplitudes and phase-shift functions [18]. This similarity complicates the determination of absolute coordination numbers, and introduces strong correlations between coordination numbers and

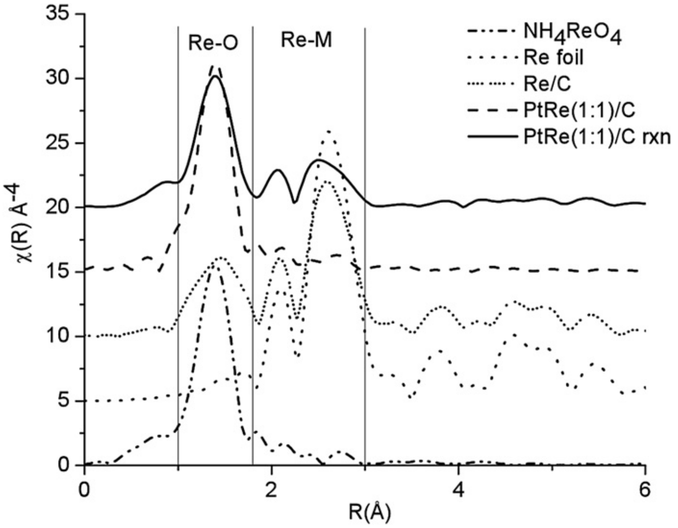

Fig. 3. Re L_{III} EXAFS Fourier transforms of catalysts (before in situ reduction). "PtRe(1:1)/C-rxn" represents a catalyst that was exposed to "harsh" reaction conditions. Spectra are offset for clarity.

Debye–Waller factors. However, some conclusions can be drawn from the qualitative description of the EXAFS data in Fig. 4 and the fitting of EXAFS functions of the monometallic samples in Fig. 5.

Fig. 4 shows the Fourier transformed EXAFS data of several catalyst samples and foil standards after in situ reduction. The amplitudes in the regions of 1.8–3.1 Å for the Re L_{III} edge and 1.9–3.5 Å for the Pt L_{III} edge decrease significantly when comparing the catalyst samples to the metal foil. The exception is the Re/C sample, which shows amplitude similar to the Re sample and is likely due to the agglomeration of Re in this sample, as described later in TEM measurements. This attenuation is indicative of a decrease in coordination ($N < 12$) as compared to the bulk metal and is consistent with the formation of nanoparticles [19]. The bimetallic samples and Pt/C also display a strong attenuation in EXAFS FT amplitude at $R > 4$ Å, which is indicative of the lack of long-range order caused by nanoparticle formation [19]. The EXAFS FT amplitude in the above-mentioned regions increases after the sample has been treated under reaction conditions, and this increase is likely due to increased first shell average coordination number caused by sintering of nanoparticles during reaction.

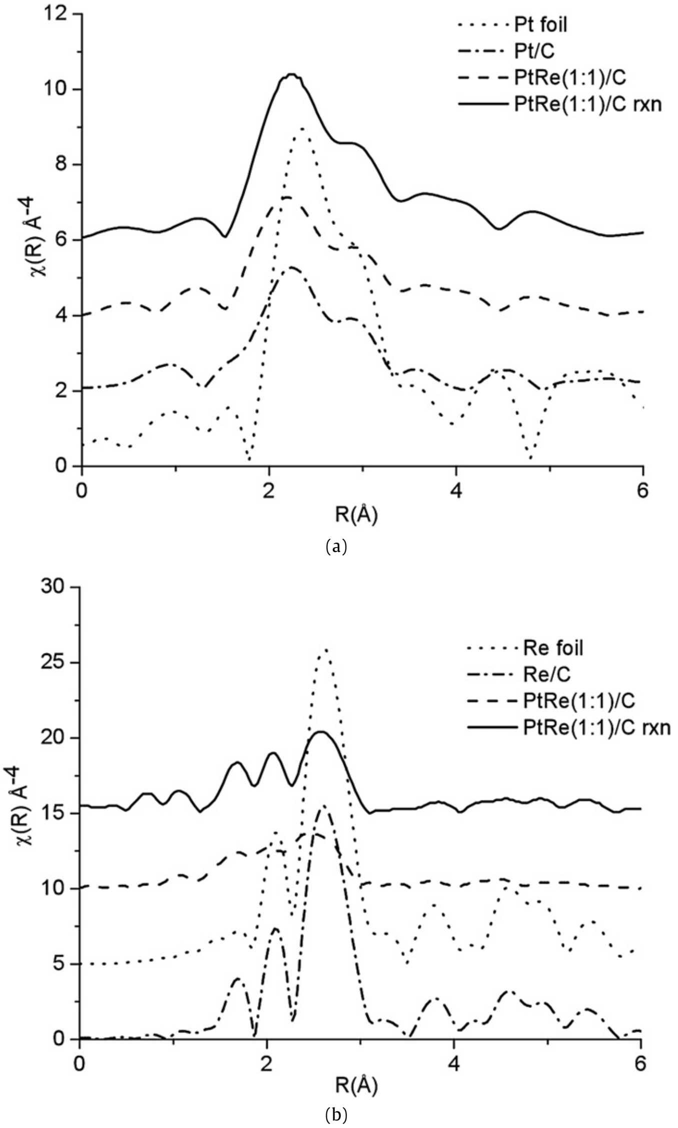

(a)

(b)

Fig. 4. (a) Pt L_{III} and (b) Re L_{III} XAFS Fourier transform of catalysts after in situ reduction. Spectra are offset for clarity.

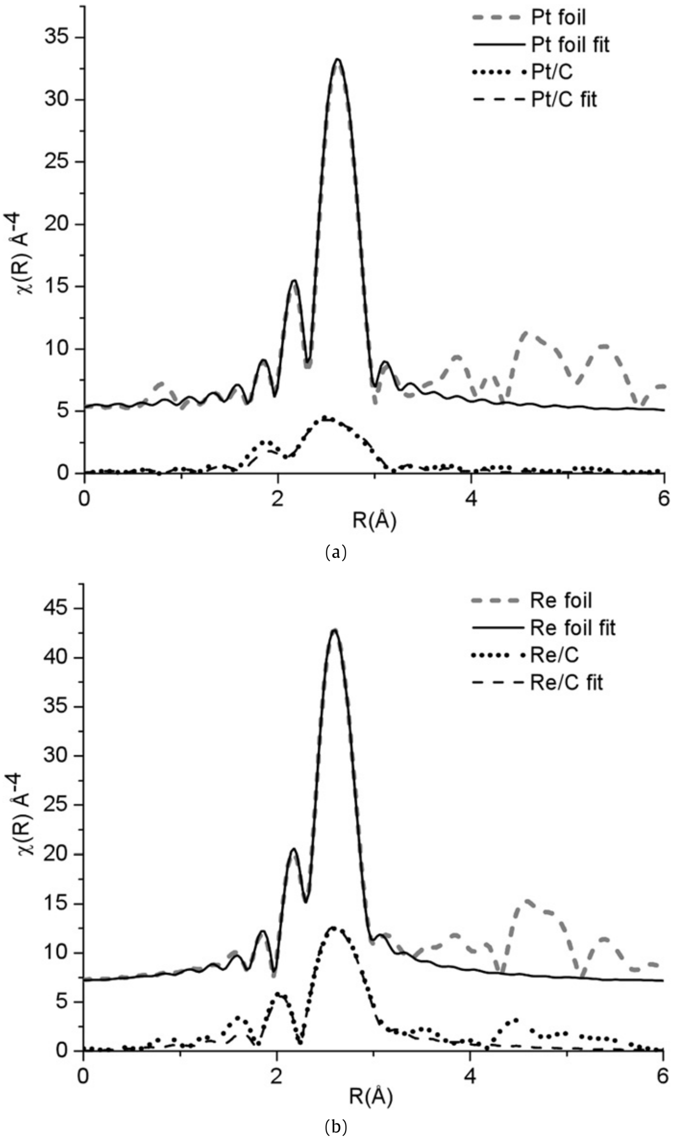

(a)

(b)

Fig. 5. Fitted k^3-weighted XAFS Fourier transforms for (a) Pt L_{III} and (b) Re L_{III}. Spectra are offset for clarity.

Table 4
Parameters from fitting of EXAFS data.

Material	FT range ΔK ($Å^{-1}$)	Fitting range ΔR (Å)	N	R (Å)	σ^2 ($Å^2$)	ΔE (eV)	S_0^2	R-factor
Pt foil	3.5–16	1.9–3.2	12	2.767 (0.002)	0.004 (0.0002)	4.0 (1.0)	0.8 (0.04)	0.05%
Pt/C	3.0–12	1.9–3.2	6.6 (1.3)	2.723 (0.009)	0.008 (0.001)	1.4 (2.0)	0.8	1.60%
Re foil	3.0–16	2.0–3.1	12	2.749 (0.001)	0.004 (0.0001)	3.3 (0.4)	0.76 (0.02)	0.04%
Re/C	3.0–13	2.0–3.0	10.5 (0.7)	2.745 (0.003)	0.005 (0.0003)	6.3 (0.8)	0.76	0.10%

EXAFS data for the monometallic catalysts and foil standards were fit in R-space using least-squares and a k^3 weighing scheme to emphasize contributions from metal back-scattering centers. The fitting range (R-space), Fourier transform range (k-space), and values of the fitted coordination (N), Debye–Waller factor (S^2), distance (R) and photoelectron energy at zero wave vector (E_0) are listed in Table 4, with the uncertainties in these parameters listed in parenthesis next to each value. The quality of the fit was calculated using the least squares residual (R-factor), and this value was lower than 2% for all cases, indicating a good fit. The amplitude reduction factors (S_0^2), extracted from the foil standards, were in agreement with those found in literature [20,21]. Comparisons of the experimental EXAFS FT data with model results using the fitted parameters are shown in Fig. 5.

The EXAFS first shell Pt–Pt and Re–Re coordination numbers are approximately 6.6 and 10.5 for the Pt/C and Re/C catalysts, respectively. The platinum coordination is comparable to that found by Zhang et al. [21] in their EXAFS study of Pt on Vulcan XC-72 carbon black. Furthermore, the Pt/C catalyst displays a significant (1.6%) contraction in the Pt–Pt bond distance, as compared to Pt foil. This contraction may be due to the increased electron density resulting from the loss of orbital hybridization in going from bulk Pt to nanoparticles [21], causing greater shielding of the positive nuclei and allowing for a smaller atomic separation. The contraction is not evident in Re/C, because of the larger particle size. Frenkel et al. have devised a correlation between the diameters of hemispherical cubohedral platinum particles and the average first shell coordination [22]. According to this correlation, the average diameters of the Pt particles in Pt/C are 1.5 nm, and metal particles greater than 4.5 nm are present in Re/C.

As mentioned previously, the Re L_{III} EXAFS FT region representing Re–metal scattering is significantly lower in magnitude for the in situ reduced Pt–Re(1:1)/C compared to Re foil and Re/C. Our attempts to fit the Re L_{III} edge of in situ reduced Pt–Re/C with either Re–Re or Re–Pt contributions show that this decrease in magnitude cannot be justified solely by undercoordination. Approximate measurements of particle size obtained from TEM and chemisorption studies provided estimates for the first shell coordination by either Pt or Re nearest neighbors. When these estimates were used to fit a coordination shell consisting of a single type of scattering atom (either Pt or Re), the fit was inadequate, suggesting a variation in the scattering atom identity and/or scattering distances in the first coordination shell. To this end, Fung et al., found that the contributions to the overall Re L_{III} EXAFS signal resulting from Re–Re and Re–Pt scattering in Al_2O_3-supported Pt–Re clusters are out of phase at high k ($k > 8$ $Å^{-1}$) [23]. Therefore, the observed decrease in EXAFS FT magnitude may result from cancellation of the Re–Re EXAFS signal by that of Re–Pt scattering, suggesting significant Pt–Re interaction caused by alloying.

3.3. Microcalorimetric measurements

The heat of CO adsorption as function of the fractional CO surface coverage is shown in Fig. 6. The fractional coverage was calculated by normalizing the actual coverage by the saturation coverage at 300 K. From Fig. 6, it can be seen that the Pt/C catalyst, with initial heat of adsorption of 115 kJ mol^{-1}, shows stronger CO adsorption sites than the pure Re catalyst, with an initial heat of adsorption of 105 kJ mol^{-1}. The Pt–Re(1:1)/C catalyst shows an initial heat of CO adsorption similar to that of Pt/C (113 kJ mol^{-1}); however, the heat of adsorption approaches that of Re/C. The heat of CO adsorption on the Pt–Re(1:2)/C catalyst is similar to that of the monometallic rhenium catalyst, suggesting that the surface is significantly modified by rhenium.

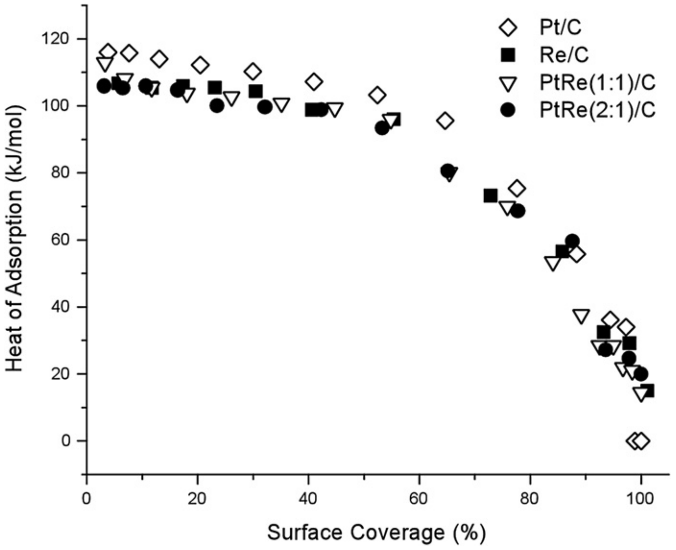

Fig. 6. Heats of CO adsorption versus fractional coverage for Pt/C, Re/C and selected PtRe/C catalysts.

It should be noted that all the catalysts display similar adsorption heat profiles. These profiles are characterized by a plateau of nearly constant heat of adsorption at low coverages followed by an abrupt decrease as the physisorption limit is reached. This behavior demonstrates that the adsorption of CO is not equilibrated and that the differential heat of CO adsorption represents an average heat from the various adsorption sites on the surface of a given catalyst particle. Therefore, it is difficult to measure the heat of adsorption specifically on the Re-modified Pt sites, which we believe are responsible for the enhanced glycerol reforming activity of the bimetallic catalyst. However, microcalorimetric data shown in Fig. 6 indicate that the average heat of CO adsorption is weakened by the presence of Re.

3.4. Temperature-programmed desorption (CO-TPD)

Temperature-programmed desorption profiles of CO from Pt/C and PtRe/C samples are shown in Fig. 7a. These profiles display maxima at 403 and 470 K, respectively, and contain broad shoulders extending to 800 K. The Re/C desorption profile contains two maxima: one at 378 K and another at 480 K. The emission of CO after 750 K results from the decomposition of functional groups found on the surface of the carbon [24,25], because CO emission in this region is observed in untreated carbon black and catalysts that have not been exposed to CO prior to the temperature ramp. The amount of CO desorbed by Pt/C, Re/C and Pt–Re(1:1)/C catalysts is consistent with CO uptake measured by static chemisorption at

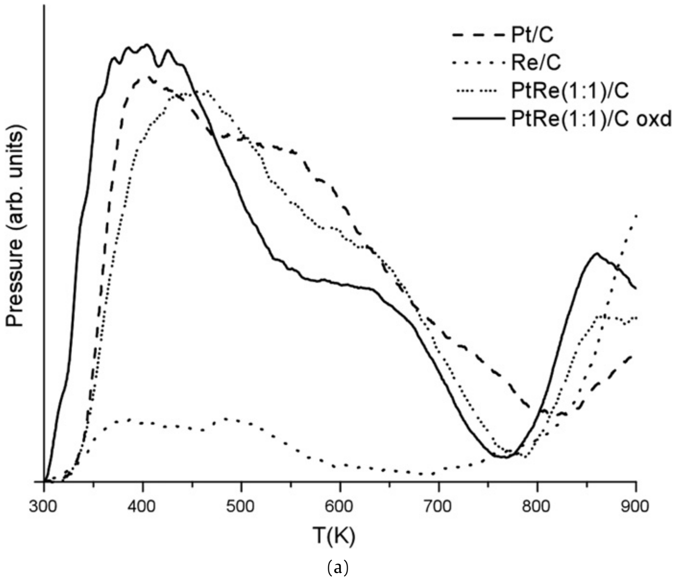

(a)

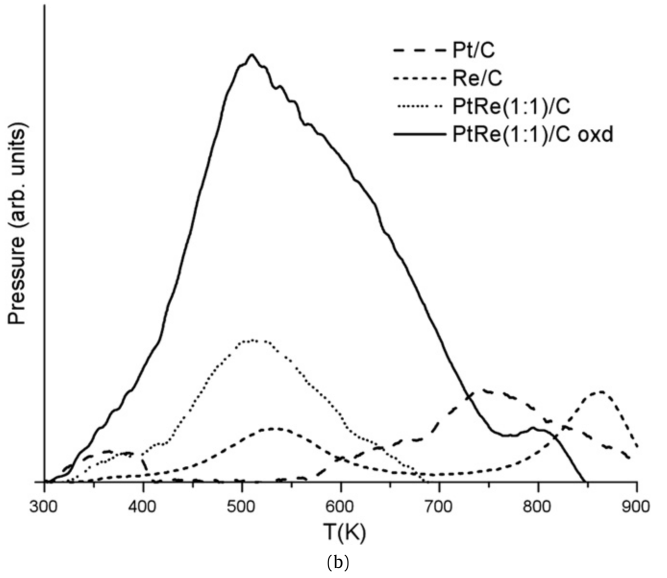

(b)

Fig. 7. (a) CO-TPD profiles and (b) associated CO_2 emission profiles for selected catalysts. "PtRe(1:1)/C oxd" represents a PtRe(1:1)/C catalysts that has undergone an oxidative pre-treatment prior to CO adsorption.

300 K. The broad peaks in the Pt/C and Pt–Re/C desorption profiles indicate that the activation energy for CO desorption varies as a function of CO surface coverage, which is normally seen for dispersed Pt [12,26]. The shift of the peak maximum to higher temperatures upon the addition of rhenium indicates the formation of adsorption sites with higher CO binding energy. This result does not necessarily contradict microcalorimetric measurements, because as mentioned previously, the heat of adsorption measured by microcalorimetry results from non-equilibrated adsorption of CO and is therefore an average of differential heats released at wide range of CO surface coverages. All catalysts display some degree of CO_2 emission during CO desorption. This emission of CO_2 has also been observed during CO-TPD of Pt/Al_2O_3, and was attributed to the reaction of adsorbed CO with hydroxyl groups on the support surface and residual moisture present in the system (Fig. 7b) [27].

Rhenium is more susceptible to oxidation than platinum [12, 16] and may become partially oxidized under reaction conditions. Based on the premise that rhenium-modified platinum sites are responsible for the enhanced activity of Pt–Re, an oxidative pre-treatment was carried out to selectively oxidize the surface rhenium, while leaving platinum in a reduced state. This pretreatment was carried out prior to the adsorption of CO, and consisted of exposing the catalyst to flowing mixture of 2 mol% O_2 in He (100 $cm^3(STP)\,min^{-1}$) at 373 K for 1 h, followed by reduction in flowing H_2 at 343 K (100 $cm^3(STP)\,min^{-1}$) and purging with He at 373 K (100 $cm^3(STP)\,min^{-1}$) for 2 h. The resulting CO desorption profile is shown in Fig. 7a. This desorption profile contains a maximum at 385 K, and CO desorption begins immediately after the start of the temperature ramp. In addition, the high-temperature shoulder (540–750 K) is decreased in area compared to that found in the desorption profiles of Pt/C and untreated Pt–Re/C. The absence of a maximum in the 480 K region indicates that surface rhenium was selectively oxidized, since both reduced Re-containing catalysts (Re/C and un-treated Pt–Re/C) contain a maximum in this region.

The above results suggest that partial oxidation of the surface may create sites with lower CO binding energy. Fig. 7b shows the CO_2 desorption profiles that accompany CO desorption from each of the four catalyst samples. The PtRe(1:1)/C catalyst, pretreated by partial oxidation, displays a significantly larger CO_2 desorption peak (510 K) than Pt/C and untreated Pt–Re/C and Re/C catalysts. This CO_2 may originate from the reduction of strongly bound oxygen (on Re sites) by CO adsorbed on neighboring Pt sites. In addition, this production of CO_2 is consistent with the higher rate of water–gas shift on PtRe catalysts.

3.5. *Transmission electron microscopy*

Transmission electron microscopy (TEM) and scanning transmission electron microscopy (STEM) studies were conducted for the samples listed in Table 1. Fresh samples (reduced and passivated prior to analysis) were examined, along with catalysts that had been exposed to glycerol reforming conditions. Representative annular dark-field (ADF) STEM images of both fresh samples and catalysts after exposure to reaction conditions are shown in Fig. 8. The Pt/C and Pt–Re/C all contain highly dispersed particles. The number density of the nanoparticles on the support was variable, with regions of the support exhibiting isolated and dispersed nanoparticles, to areas that were densely populated by nanoparticles. In some cases, the particle density was so high that the nanoparticles appeared almost contiguously arranged in projection. In addition to the nanoparticles, some catalysts contained obvious areas of agglomeration. The agglomerates on the monometallic Re have a dendritic morphology; two examples are presented in Fig. 10b. Qualitative observations during TEM analysis suggest that the number density and size of the agglomerates increased with the increasing Re loading.

Particle size distributions for Pt/C, Pt–Re(1:1)/C, and Pt–Re (1:2)/C both before and after reaction are shown in Fig. 9. These distributions were generated using ADF images and only include nanoparticles that were isolated on the support, agglomerates and overlapping nanoparticles were neglected. In addition to the exclusion of large agglomerates, single atoms, dimers, trimers, and very small clusters of atom were also excluded from the distributions due to the difficulty in resolving these entities. The measurements were made using a pixel edge length between 0.05 and 0.20 nm, and ~125 particles were included in each distribution. The monometallic Pt/C has an average particle size of 1.38 ± 0.43 nm. The addition of Re increases the average particle size to 1.62 ± 0.38 nm for a 1:1 Pt:Re ratio and to 1.74 ± 0.35 for a 1:2 Pt:Re ratio. After reaction under clean conditions, the particle size for Pt/C nearly doubles to 2.26 ± 0.43 nm, whereas the particle size of the Pt–Re(1:1)/C remains similar after exposure to clean reaction conditions (with an average diameter increase of only 0.21 nm).

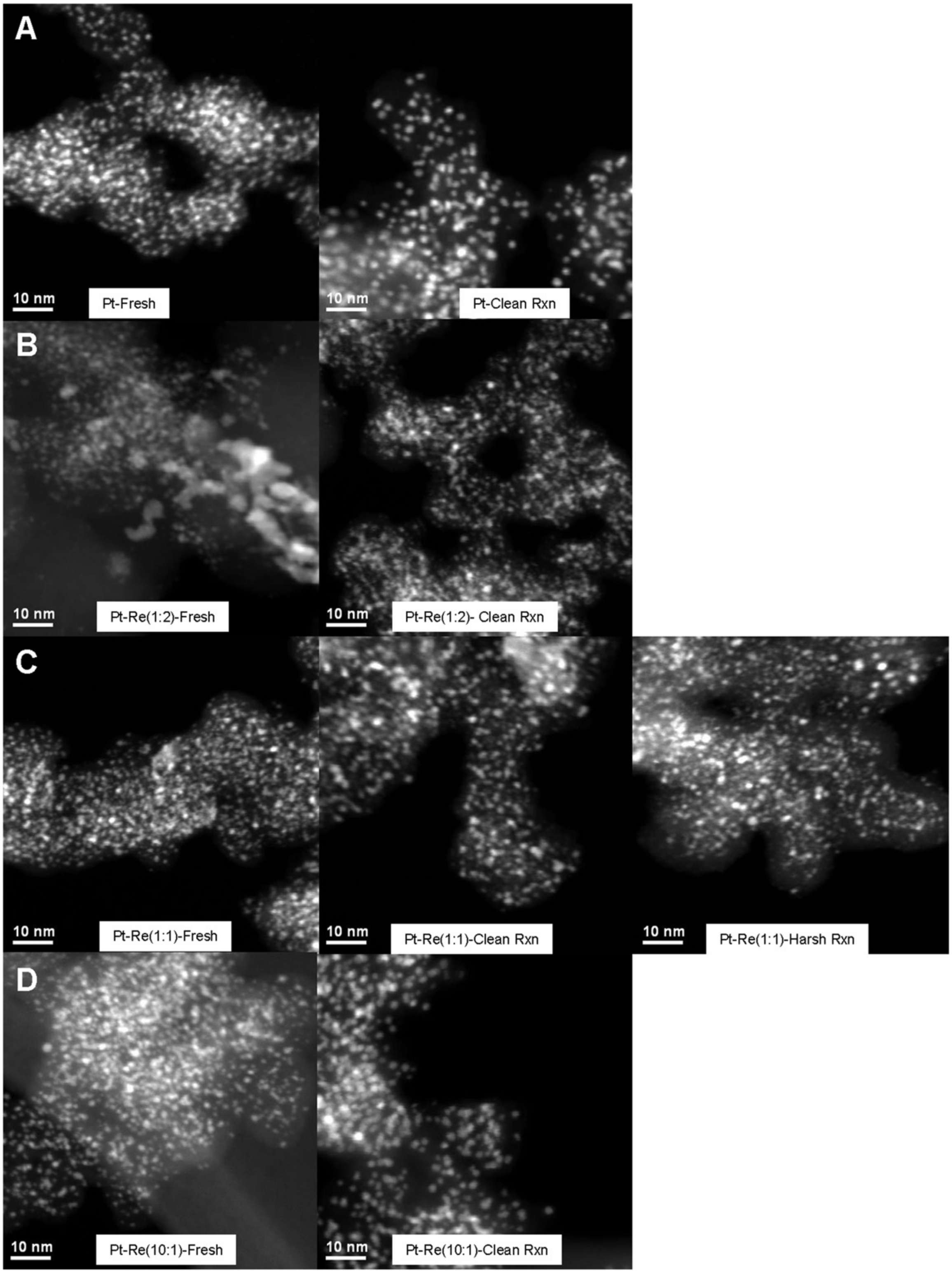

Fig. 8. Representative ADF STEM images of (A) 5 wt% Pt/C, (B) 3.4 wt% Pt–6.6 wt% Re/C, (C) 5.1 wt% Pt–4.9 wt% Re/C, and (D) 5.1 wt% Pt–0.5 wt% Re/C. Images to the right show each sample after exposure to clean reaction conditions. Pt–Re(1:1)/C was also imaged following exposure to harsh reaction conditions.

Exposure to harsh reaction conditions causes the particles on the Pt–Re(1:1)/C to significantly increase in size from 1.62 ± 0.38 to 2.23 ± 0.88 nm. These results suggest that the addition of Re helps to stabilize the nanoparticles or the support surface such that sintering was limited during reaction under clean conditions.

Energy dispersive spectroscopy (EDS) was used to analyze the compositions of the nanoparticles. Figs. 10–13 show EDS spectra (with the corresponding ADF STEM image showing the scan area) for the fresh catalyst samples. As expected, the Pt/C and Re/C showed the presence of only Pt and Re, respectively. Fig. 14 shows the complete labeled EDS spectrum of a large area scan of fresh PtRe(1:1), showing the Pt and Re L lines, whose intensities were used in the interpretation of EDS results. The oxygen peak at 0.5 eV is likely due to a Re-oxide or from functionalized groups

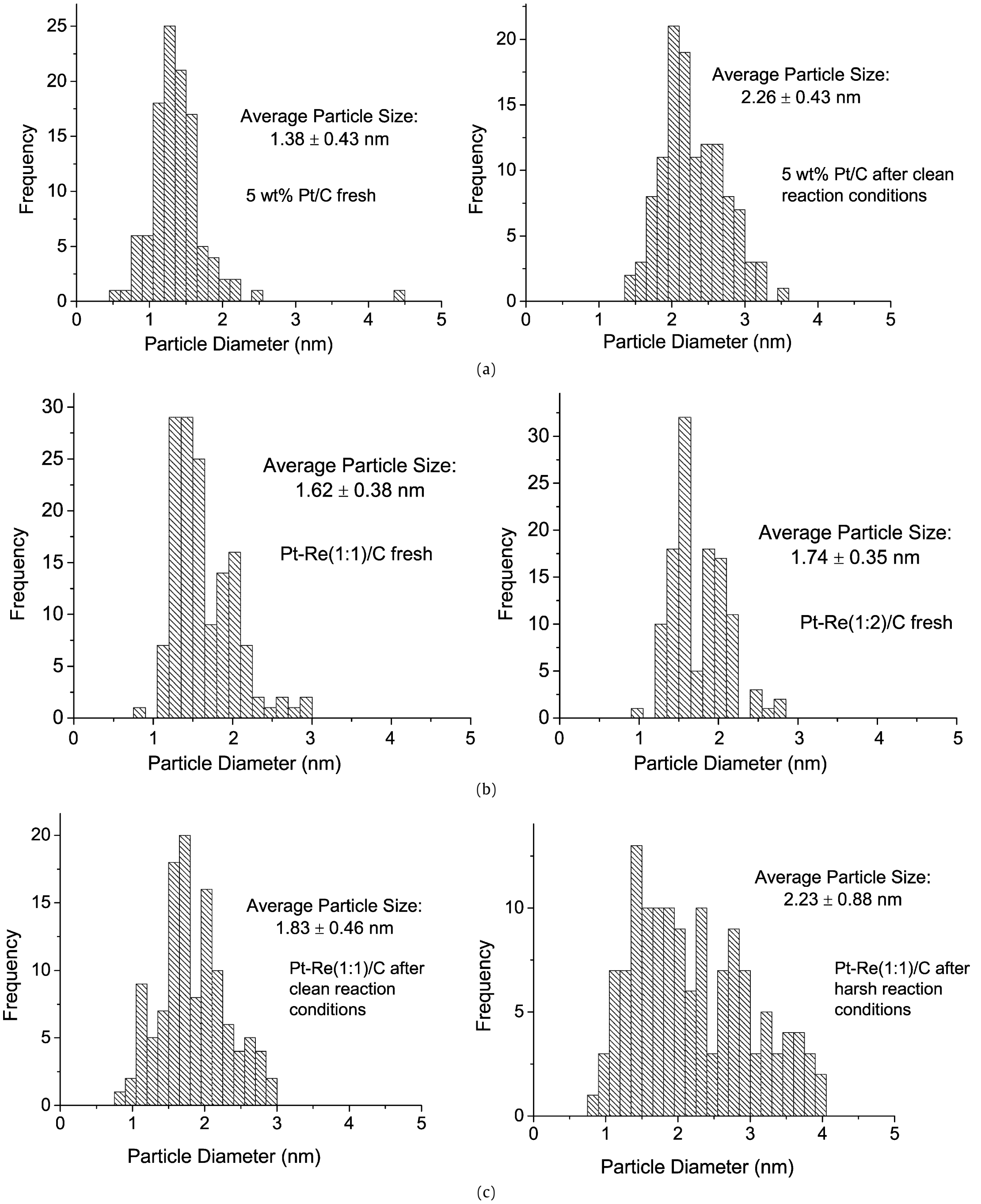

Fig. 9. Particle size distributions for (a) fresh 5 wt% Pt/C and 5 wt% Pt/C after exposure to clean reaction conditions, (b) fresh 5.1 wt% Pt–4.9 wt% Re/C and fresh 3.4 wt% Pt–6.6 wt% Re, and (c) 5.1 wt% Pt–4.9 wt% Re/C after exposure to harsh and clean reaction conditions.

that are known to exist on Vulcan carbon supports. The observation of oxygen in the large area EDS scans also corresponds directly with the regions showing the highest nanoparticle densities. This result suggests that functional groups on the support carbon are necessary for dense nanoparticle populations that remain well dispersed.

Large-area scans of the Pt–Re(1:2)/C (Fig. 11) show evidence of well-dispersed bimetallic particles (spectra 1–4) since each spectrum shows peaks for both Pt and Re, whereas the agglomerates (spectra 6 and 7) appear to contain only Re. The Pt/Re peak ratio is similar for each of the particle clusters, suggesting uniform average composition within each scan area. One particularly large particle (spectrum 5) appears to contain primarily Re, with only a small Pt peak at 9.5 eV. Similarly, the EDS scans of particle clusters in Pt–Re(1:1)/C (Fig. 12) consistently show the presence of both metals. The Pt signal is higher compared to that of the Pt–Re(1:2)/C, confirming the expected increase in Pt:Re ratio. Single particle analyses of fresh Pt–Re(1:1)/C show bimetallic Pt–Re particles with enrichment of Pt (∼70% using the standard-less quantification technique). This Pt enrichment is inconsistent with the bulk composition determined by large area scans that averaged thousands of nanoparticles. However, Anderson, et al. reported similar results for 20 wt% Pt–Re (Pt:Re = 1:1) on carbon black and suggested that the Pt enrichment results from vaporization of volatile Re surface oxides by the intense stationary electron beam during EDS analysis [28]. This effect is likely the case in this study since nanoparticles exposed to the stationary STEM probe for long times exhibited significant deformation. For the same catalyst after expo-

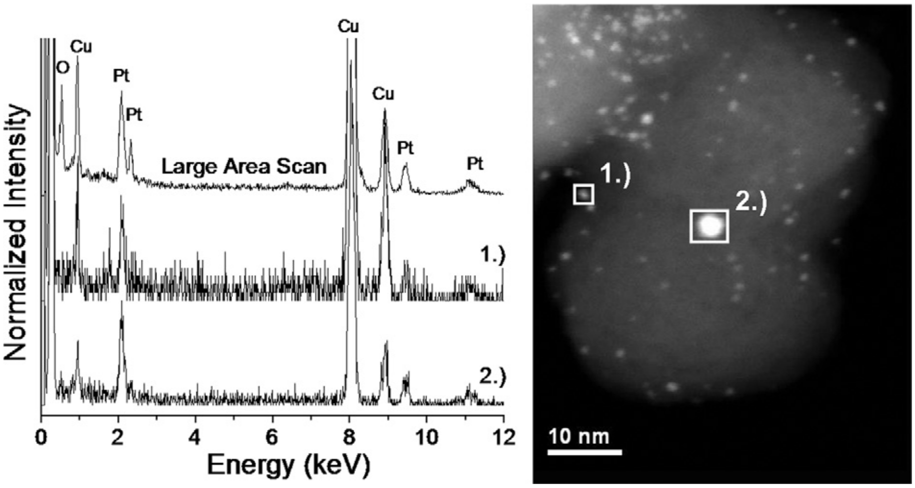

(a)

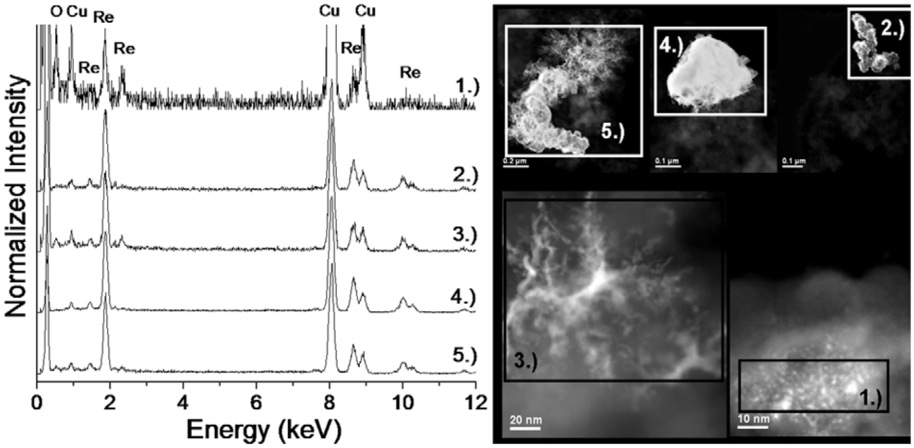

(b)

Fig. 10. EDS spectra and corresponding ADF STEM images of scanned areas for (a) fresh 5.0 wt% Pt/C and (b) fresh 5.0 wt% Re/C after reduction/passivation treatment. The numbered rectangular box corresponds directly with the same numbered spectrum in the plot to identify the area of interest from which the EDS spectrum was collected.

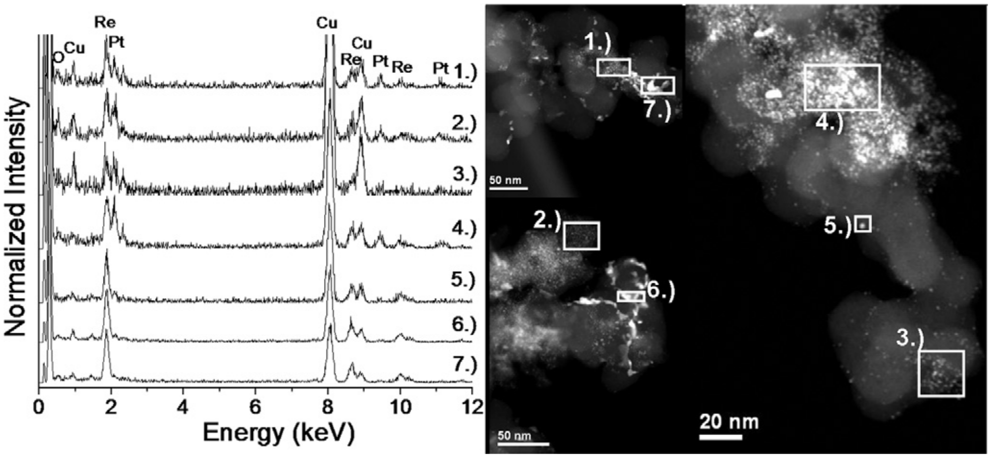

Fig. 11. EDS spectra and corresponding ADF STEM images of scanned areas for fresh 3.4 wt% Pt–6.6 wt% Re/C (Pt:Re = 1:2) after reduction/passivation treatment. The numbered rectangular box corresponds directly with the same numbered spectrum in the plot to identify the area of interest from which the EDS spectrum was collected.

sure to harsh reactions conditions, two different particle compositions were observed in the Pt–Re(1:1)/C. The first composition was Pt-rich bimetallic nanoparticles observed in the fresh sample, and the second composition consists almost entirely of Re and typically had a much larger particle size (∼10 nm). Finally, as expected, the spectra for the Pt–Re(10:1)/C (Fig. 13) contain predominantly Pt, and in some areas show trace Re signal (spectrum 2).

The results of TEM imaging and EDS analysis for the fresh samples (reduced and passivated) indicate that Pt is better dispersed on the carbon support than is Re, and the addition of Re (∼ equimolar or greater) to Pt leads to the formation of bimetallic particles. Under oxidizing conditions, the rhenium contained in these bimetallic particles becomes extensively oxidized, and the oxidation likely proceeds into the bulk of the particles. Based on

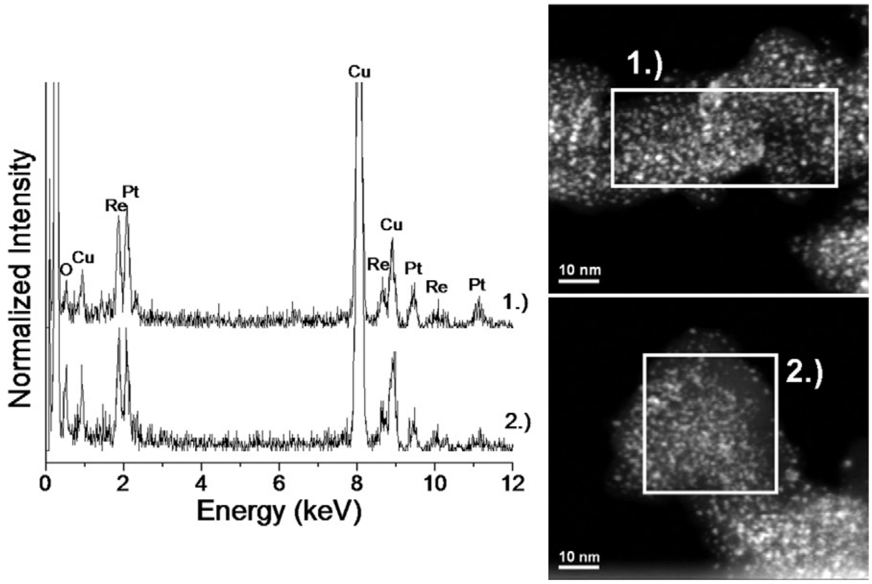

Fig. 12. EDS spectra and corresponding ADF STEM images of scanned areas for fresh 5.1 wt% Pt–4.9 wt% Re/C (Pt:Re = 1:1) after reduction/passivation treatment. The numbered rectangular box corresponds directly with the same numbered spectrum in the plot to identify the area of interest from which the EDS spectrum was collected.

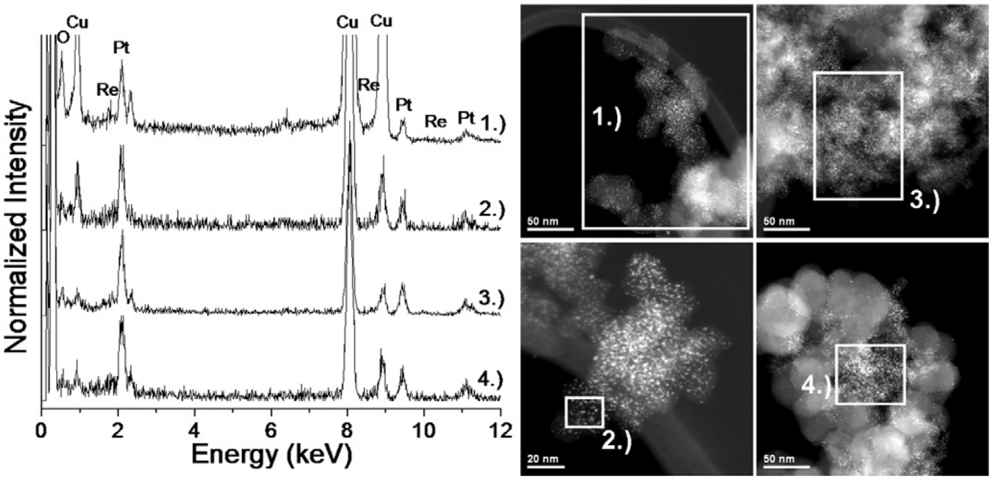

Fig. 13. EDS spectra and corresponding ADF STEM images of scanned areas for fresh 5.1 wt% Pt–0.5 wt% Re/C (Pt:Re = 10:1) after reduction/passivation treatment. The numbered rectangular box corresponds directly with the same numbered spectrum in the plot to identify the area of interest from which the EDS spectrum was collected.

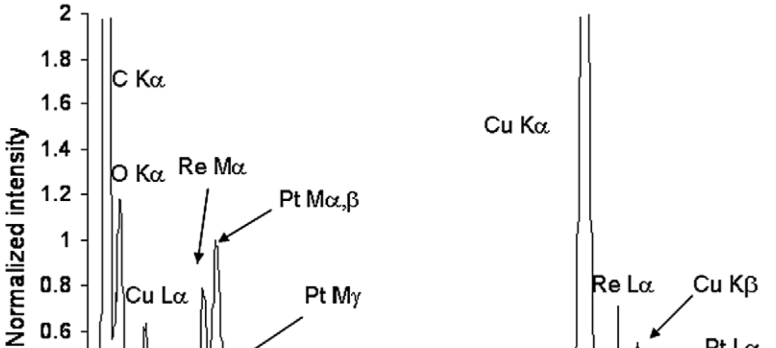

Fig. 14. Large area EDS scan of fresh 5.1 wt% Pt–4.9 wt% Re/C.

the XAS and CO-TPD data, the EDS results could be interpreted as indicating that Pt nanoparticles are covered with, are adjacent to, or contain Re–O moieties that directly interact with the Pt; and, these Re–O moieties are readily oxidized and reduced depending on the surrounding environment. Increasing the Re content or exposure to harsh reaction conditions can lead to formation of large Re agglomerates along with well-dispersed nanoparticles that are either bimetallic or have Re and Pt in close proximity such that they appear together in EDS spectra. Comparisons of ADF STEM images (Fig. 8) and particle size distributions (Fig. 9) for the Pt/C and Pt–Re/C samples before and after exposure to reaction conditions reveals that the crystallites undergo sintering during reaction as evidenced by the increase in particle size in each case. Monometallic Pt exhibits the most significant sintering, where the average nanoparticle size nearly doubled; addition of Re appears to suppress nanoparticle sintering resulting in only marginal increases in average particle size. EDS scans of large areas exposed to reaction conditions were similar to fresh samples, suggesting that the overall compositions were unaffected by reaction conditions.

There have been several reports of formation of bimetallic phases on Al_2O_3-supported Pt–Re catalysts, each concluding that platinum-catalyzed reduction of highly mobile Re oxide species results in alloy formation and that Re oxide mobility increases with support hydration [12,29,30]. Highly dehydrated alumina is known to strongly interact with the Re oxide species, leading to the formation of highly dispersed Re oxide that disrupts alloy formation [30]. The TEM evidence presented here suggests the incorporation of Re into highly dispersed alloyed nanoparticles, although we cannot definitively exclude the possibility that they the metals are in very close proximity without alloying. These Pt–Re nanoparticles are responsible for the enhanced activity of the catalyst as compared to neat Pt. Without Pt, a majority of the surface Re-oxides retain their mobility, reducing at higher temperatures and forming large metallic agglomerates. A smaller fraction of the Re may interact with oxidic surface groups on the carbon support, forming smaller particles (analogous to dispersion of Re on dehydrated alumina). Conditions such as high partial pressures of water may lead to the formation of mobile Re oxides [31] causing Re segregation and thus disrupting the association with Pt.

4. Nature of active sites for glycerol conversion

The results of reaction kinetics measurements and characterization studies indicate that Pt and Re are in close contact within Pt–Re/C catalysts. These studies show an increase in overall activity as well as an increase in the rate of water–gas shift. XAS and TEM studies suggest the presence of Pt–Re interaction in the Pt–Re/C catalysts, while CO-TPD and microcalorimetry studies suggest that Re alters the Pt surface. Additionally, CO-TPD of a partially oxidized Pt–Re catalyst reveals the formation of surface sites with lower CO binding energies as compared to Pt/C and Re/C.

Results from density functional theory (DFT) calculations suggest that cleavage of C–C bonds on Pt for an oxygenated hydrocarbon takes place through transition states that have lower energy and are more dehydrogenated compared to transition states for cleavage of C–O bonds [32]. Because these transition states are multiply bonded to the surface, the rate of C–C bond cleavage is expected to be highly dependent on the coverages by abundant adsorbed species that block surface sites, such as adsorbed CO and various other reaction intermediates. Accordingly, the higher catalytic activity of Pt–Re catalysts (compared to Pt) for production of H_2 and CO from glycerol reforming may be caused by less extensive blocking of surface sites by reaction intermediates and/or products. This assertion is based on our results from microcalorimetric and TPD studies indicating that one of the effects of Re in Pt–Re catalysts is to weaken the strength of CO adsorption. In addition, Re can promote the rate of the reforming reaction by removing adsorbed CO species from the surface by facilitating the water–gas shift reaction [33], as well as by achieving hydrogenolysis of C–O bonds in oxygenated hydrocarbons. The increased rate of water–gas shift caused by addition of Re to Pt is evidenced in the present study by a significant decrease in the CO/CO_2 ratio, and an increased rate of C–O hydrogenolysis under harsh reaction conditions is evidenced by a decrease in the CO/C_{alkane} ratio. Because the binding energies of oxygen atoms and hydroxyl groups are stronger on Re than on Pt [34], these effects of Re on the catalytic properties of PtRe-based catalysts may be caused by the presence of oxygen species, for example hydroxyl groups, associated with Re atoms on the surface of Pt–Re particles, as outlined in Fig. 15.

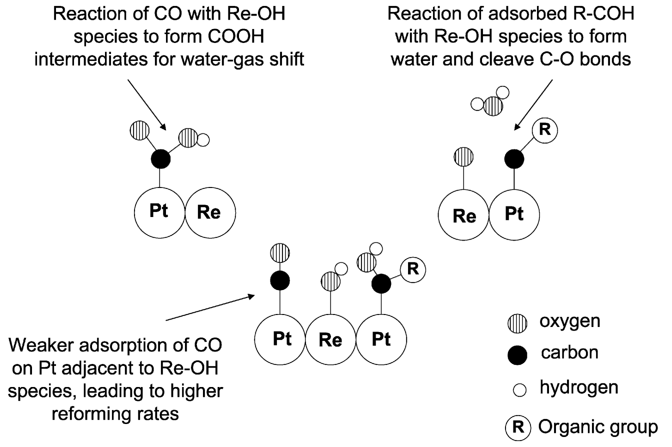

Fig. 15. Schematic representation for effects of Re–OH species on the catalytic properties of Pt–Re catalysts for reforming of oxygenated hydrocarbons.

Results from DFT calculations show that the –OH group on the central Re surface atom in Fig. 15 is predicted to weaken the strength of CO adsorption on the neighboring surface Pt atom, thereby lowering the CO coverage on Pt-sites during reforming reactions at low temperatures (e.g. 500 K), leading to higher rates of formation of $CO/CO_2/H_2$ gas mixtures from oxygenated hydrocarbons [35]. These –OH groups on Re may also react with CO adsorbed on neighboring Pt sites (the left portion of Fig. 15), leading to the formation of –COOH species, which are reactive intermediates for the water–gas shift reaction on Pt [36]. In addition, the –OH group on Re may serve as a hydrogen transfer agent for reaction with hydroxyl groups in oxygenated hydrocarbon species associated with neighboring Pt sites (the right portion of Fig. 15), leading to cleavage of the C–OH bond by dehydration of the oxygenated hydrocarbon.

The sketch in Fig. 15 for Pt–Re-based catalysts is consistent with the effects on the catalytic properties of increasing the system pressure for glycerol reforming. From the results discussed previously, increasing the system pressure decreases the $CO:CO_2$ ratio and shifts the product selectivity for glycerol reforming towards alkanes and oxygenated hydrocarbons at the expense of CO/CO_2. In particular, higher system pressures and lower system temperatures lead to higher partial pressures and higher surface coverages by the CO and hydrogen products from reforming. Because the transition states for reforming reactions are multiply bonded to the surface and thus require multiple surface Pt atoms, the higher coverages by adsorbed products inhibit the rate of C–C bond cleavage. In addition, the higher pressure of hydrogen may also inhibit the rate of C–C bond cleavage during glycerol reforming over Pt by shifting the equilibrium away from the hydrogen-deficient adsorbed intermediates that lead to cleavage of C–C bonds. In contrast, the rate of water–gas shift over Pt–Re would be less sensitive to system pressure, because Re–OH surface sites would not be poisoned by higher pressures of CO as evidenced by the decrease in the $CO:CO_2$

ratio at higher system pressures. This effect is analogous to the behavior of water–gas shift on supported metal catalysts containing reducible oxide supports, where CO adsorption on Pt does not inhibit the rate of water dissociation on the reducible support, and the rate of the overall reaction is thus uninhibited by CO at elevated pressures [37]. This same behavior also explains why the selectivity toward alkanes and oxygenated hydrocarbons for glycerol reforming over Pt–Re increases at higher system pressures. Specifically, the rate of C–C bond cleavage and thus formation of $CO/CO_2/H_2$ from glycerol is slower at higher pressures of CO and H_2, whereas the formation of alkanes and oxygenated hydrocarbons from glycerol involves the participation of hydroxyl groups associated with Re, which is not highly dependent on system pressure.

5. Conclusions

Results from reaction kinetics measurements show that Pt–Re/C catalysts are more active for glycerol conversion compared to monometallic Pt/C. Furthermore, these results suggest that the addition of Re to Pt increases the rates of the water–gas shift reaction as well as alkane formation reactions. Microcalorimetric and CO-TPD studies reveal surface modification resulting from addition of Re to Pt. In particular, CO-TPD demonstrates that the desorption energy of CO on Pt–Re/C decreases relative to the monometallic samples after exposure to a selectively oxidative pretreatment. This selective oxidation of surface Re may occur under reaction conditions, and is potentially responsible for the formation of active surface sites. X-ray adsorption spectroscopy and TEM studies suggest that Pt–Re catalysts consist of bimetallic alloy nanoparticles. Exposure to reaction conditions leads to slight sintering and segregation of Re. Importantly, Re appears to help alleviate sintering of Pt. These results suggest that Re participates in glycerol conversion by weakening the binding energy of CO to neighboring Pt sites, increasing the rate of water–gas shift, and facilitating hydrogenolysis of C–O bonds at elevated pressures; these effects can be explained in terms of active sites consisting of Pt surface atoms adjacent to Re surface atoms that preferentially bond to oxygen species, such as hydroxyl groups.

Acknowledgments

This work was supported by the U.S. Department of Energy (DOE), Office of Basic Energy Sciences, Chemical Sciences Division. Use of the National Synchrotron Light Source, Brookhaven National Laboratory, for the EXAFS experiments was supported by the U.S. Department of Energy (DOE/BES Grant No. DE-FG02-05ER15688). W.D.P. and D.J.B. thank Chaoying Ni and Frank Kriss with the Keck Electron Microscopy Facility for EM assistance. We also thank Professor Manos Mavrikakis for valuable discussions and collaborations throughout this project.

References

[1] D.L. Klass, Biomass for Renewable Energy, Fuels, and Chemicals, Academic Press, San Diego, 1998.
[2] D.A. Simonetti, E.L. Kunkes, J.A. Dumesic, J. Catal. 247 (2007) 298–306.
[3] R.R. Soares, D.A. Simonetti, J.A. Dumesic, Angew. Chem. Int. Ed. 45 (2006) 3982–3985.
[4] D.A. Simonetti, E.L. Kunkes, J. Rass-Hansen, R.R. Soares, J.A. Dumesic, Green Chem. 9 (2007) 1073–1083.
[5] M.S. Nashner, A.I. Frenkel, D. Somerville, C.W. Hills, J.R. Shapley, R.G. Nuzzo, J. Am. Chem. Soc. 120 (1998) 8093–8101.
[6] R. Gordon, Preparing Samples for XAFS Data Collection, Argonne, IL, USA, 2007.
[7] B. Ravel, M. Newville, J. Synch. Rad. 12 (2005) 537–541.
[8] R. MacGivallry, in: K. Lonsdale (Ed.), International Tables of X-Ray Crystallography, vol. III, Kynoch, Birmingham, 1962.
[9] B.E. Spiewak, J. Shen, J.A. Dumesic, J. Phys. Chem. 99 (1995) 17640.
[10] R.D. Cortright, R.R. Davda, J.A. Dumesic, Nature 418 (2002) 964–967.
[11] R.R. Davda, J.W. Shabaker, G.W. Huber, R.D. Cortright, J.A. Dumesic, Appl. Catal. B Environ. 43 (2003) 13–26.
[12] F. Hilbrig, C. Michel, G.L. Haller, J. Phys. Chem. 96 (1992) 9893–9899.
[13] T. Ressler, J. Wienold, R.E. Jentoft, T. Neisius, J. Catal. 210 (2002) 67–83.
[14] J.G. Chen, B. Fruhberger, M.L. Colaianni, J. Vac. Sci. Technol. A 14 (1996) 1668.
[15] J.G. Chen, C.M. Kim, B. Fruhberger, B.D. DeVries, M.S. Touvelle, Surf. Sci. 321 (1994) 145.
[16] W.T. Tysoe, F. Zaera, G.A. Somorjai, Surf. Sci. 200 (1988) 1–14.
[17] M. Ronning, T. Gjervan, R. Prestvik, D.G. Nicholson, A. Holmen, J. Catal. 204 (2001) 292–304.
[18] C.G. Michel, W.E. Bambrick, R.H. Ebel, G. Larsen, G.L. Haller, J. Catal. 154 (1995) 222–229.
[19] B.K. Teo, EXAFS Spectroscopy: Techniques and Applications, Plenum Press, New York, 1980.
[20] N.M. Yang, G.E. Mickelson, N. Greenlay, S.D. Kelly, F.D. Vila, J. Kas, J.J. Rehr, S.R. Bare, Size and shape of rhenium nanoparticles, 2007.
[21] Y.H. Zhang, M.L. Toebes, A. van der Eerden, W.E. O'Grady, K.P. de Jong, D.C. Koningsberger, J. Phys. Chem. B 108 (2004) 18509–18519.
[22] A.I. Frenkel, C.W. Hills, R.G. Nuzzo, J. Phys. Chem. B 105 (2001) 12689–12703.
[23] A.S. Fung, M.J. Kelley, D.C. Koningsberger, B.C. Gates, J. Am. Chem. Soc. 119 (1997) 5877–5887.
[24] A. Guerrero-Ruiz, P. Badenes, I. Rodriguez-Ramos, Appl. Catal. A 173 (1998) 313–321.
[25] A. Sepulveda-Escribano, F. Coloma, F. Rodriguez-Reinoso, Appl. Catal. A 173 (1998) 247–257.
[26] P. Thormahlen, M. Skoglundh, E. Fridell, B. Andersson, J. Catal. 188 (1999) 300–310.
[27] K. Foger, J.R. Anderson, Appl. Surf. Sci. 2 (1979) 335–351.
[28] A.D. Anderson, G.A. Deluga, J.T. Moore, M.J. Vergne, D.M. Hercules, E.A. Kenik, C.M. Lukehart, J. Nanonsci. Nanotechnol. 4 (2004) 809.
[29] P. Malet, G. Munuera, A. Caballero, J. Catal. 115 (1989) 567–579.
[30] R. Prestvik, B. Totdal, C.E. Lyman, A. Holmen, J. Catal. 176 (1998) 246–252.
[31] M.Yu. Smirnov, A.R. Cholach, V.A. Sobyanin, V.V. Gorodetskii, Poverkhnost 6 (1983) 132–139.
[32] R. Alcala, M. Mavrikakis, J.A. Dumesic, J. Catal. 218 (2003) 178–190.
[33] Y. Sato, K. Terada, S. Hasegawa, T. Miyao, S. Naito, Appl. Catal. A Gen. 296 (2005) 80–89.
[34] J.L. Zhang, M.B. Vukmirovic, K. Sasaki, A.U. Nilekar, M. Mavrikakis, R.R. Adzic, J. Am. Chem. Soc. 127 (2005) 12480–12481.
[35] J. Greeley, M. Mavrikakis, Catal. Today 111 (2005) 52–58.
[36] A.B. Mhadeshwar, D.G. Vlachos, J. Phys. Chem. B 108 (2004) 15246–15258.
[37] A.A. Phatak, N. Koryabkina, S. Rai, J.L. Ratts, W. Ruettinger, R.J. Farrauto, G.E. Blau, W.N. Delgass, F.H. Ribeiro, Catal. Today 123 (2007) 224–234.